Overview of Recent Experimental Results on MAST

B. Lloyd 1), J-W. Ahn 2), R.J. Akers 1), L.C. Appel 1), E.R. Arends 3), K.B. Axon 1), R.J. Buttery 1), C. Byrom 4), P.G. Carolan 1), C. Challis 1), D. Ciric 1), N.J. Conway 1), M. Cox 1), G.F. Counsell 1), G. Cunningham 1), A. Darke 1), A. Dnestrovskij 5), J. Dowling 1), M.R. Dunstan 1), A.R. Field 1), S.J. Fielding 1), S. Gee 1), M.P. Gryaznevich 1), P. Helander 1), M. Hole 1), M.B. Hood 1), P.A. Jones 2), A. Kirk 1), I.P. Lehane 6), G.P. Maddison 1), S.J. Manhood 1), R. Martin 1), G.J. McArdle 1), K.G. McClements 1), M.A. McGrath 7), H. Meyer 1), A.W. Morris 1), S.K. Nielsen 8), M. Nightingale 1), A. Patel 1), T. Pinfold 1), M.N. Price 1), J. Qin 2), C. Ribeiro 1), C.M. Roach 1), D.C. Robinson 1), O. Sauter 9), V. Shevchenko 1), S. Shibaev, 1) K. Stammers 1), A. Sykes 1), A. Tabasso 1), D. Taylor 1), M.R. Tournianski 1), G. Turri 2), M. Valovic 1), G. Voss 1), M.J. Walsh 10), S. Warder 1), J.R. Watkins 1), H.R. Wilson 1), Y. Yang 11), S. You 2) and the MAST and NBI teams.

1) EURATOM/UKAEA Fusion Association, Culham Science Centre, Abingdon, Oxfordshire OX14 3DB, UK
2) Imperial College of Science, Technology and Medicine, London SW7 2BZ, UK
3) FOM Instituut voor Plasmafysica Rijnhuizen, Nieuwegein, Netherlands
4) University of Manchester Institute of Science & Technology, Manchester, UK
5) Kurchatov Institute, Moscow, Russia
6) University College, Cork , Ireland
7) University College, Dublin, Ireland
8) University of Aarhus, Denmark
9) CRPP, Association Euratom – Confederation Suisse, EPFL, 1015 Lausanne, Switzerland
10) Walsh Scientific Ltd, Culham Science Centre, Abingdon, OX14 3EB, UK
11) Institute of Plasma Physics, Hefei, 230031, P.R. China
e-mail contact of main author: brian.lloyd@ukaea.org.uk

Abstract. The low aspect ratio of MAST allows differentiation between different forms of the H-mode threshold scaling. With optimised fuelling (inboard puffing) and magnetic configuration (connected DND) the H-mode power threshold data lie somewhat above (~ x1.7) recent scaling laws. Slight magnetic configuration changes (of the order of the ion Larmor radius) around a connected DND significantly influence H-mode access. H-mode confinement in discharges with low frequency ELMs is generally consistent with the IPB98(y,2) scaling. Strong indications of both particle and energy internal transport barriers have been seen. Normalised beta values $\beta_N > 5$ have been obtained, approaching the ideal n = 1 no wall external kink stability limit. Sawtooth triggered NTMs (3/2, 2/1) have been observed; numerical modelling of the island evolution reproduces mode behaviour well and confirms the significance of stabilising field curvature effects. Divertor power loading studies, including transient effects (e.g. due to ELMs), show a strong bias of power efflux to the outboard targets where it is more easily handled. ELM energy losses ΔW_{ELM} are less than 4% of the stored energy in all regimes explored so far, but ELM effluxes extending 30cm outside the outboard separatrix have been measured. Toroidally asymmetric divertor biasing resulted in significant broadening of the D_α profile on the biased components and a reduction in the total power to the unbiased components. Halo current magnitudes and asymmetries are generally small compared with conventional tokamaks; recent measurements show that the plasma behaves more as a voltage source than a current source. Initial neutral beam current drive experiments indicate non-inductively driven current values ($I_{NBI} \sim 0.3 I_p$) comparable with code predictions.

1. Introduction

The Mega Amp Spherical Tokamak (MAST) is a second generation spherical tokamak (ST) designed to study low collisionality, low aspect ratio (R/a ~ 1.3), highly elongated ($\kappa > 2$) plasmas with a plasma current and poloidal cross-section comparable to medium sized

conventional tokamaks such as DIII-D and ASDEX-U. It is equipped with high power NBI (5MW) and ECRH (1.4MW) heating systems, adaptable fuelling systems (both outboard and inboard gas puffing plus a multi-pellet injector) and benefits from an extensive array of advanced diagnostics. These include:

- dual Thomson scattering systems comprising of a *300 spatial point* ruby laser system covering both core and pedestal regions and a multi-pulse NdYAG system;
- active and passive charge exchange spectroscopy giving profiles of ion temperature and toroidal velocity;
- a *200 chord* visible bremsstrahlung diagnostic for Z_{eff} profiles;
- advanced spectroscopic diagnostics giving profiles of T_e, n_e, toroidal velocity ($v_{\phi i}$) and neutral density (n_0) in the pedestal region;
- a neutral particle analyser with both *toroidal and poloidal scanning capability* to monitor fast ion behaviour;
- comprehensive edge diagnostics to monitor divertor targets (*> 500 Langmuir probes* plus thermocouples), a reciprocating probe for mid-plane scrape-off layer measurements and infra-red thermography;
- comprehensive halo current measurements (*176 detectors*).

High purity plasma conditions are ensured by high temperature baking, periodic boronisation and inter-shot helium glow discharge cleaning. MAST parameters are summarised in Table I.

	Design	Achieved
Minor & Major radii a, R (m)	0.65, 0.85	0.65, 0.85
Elongation κ	≥ 2	2.45
Aspect ratio A	≥ 1.3	1.3
Plasma Current I_p (MA)	2	1.35
Toroidal Field $B_{\phi 0}$ (T) at R	0.52	0.52
Aux. Heating: P_{NBI} (MW)/P_{ECH} (MW)	5/1.4	3/0.6
Pulse length (s)	5	0.7

TABLE I MAST PARAMETERS

The experimental programme concentrates on addressing key physics issues for ITER and on further exploring the potential of the spherical tokamak concept, in order to establish its viability as a prospective fusion materials test facility and/or power plant.

2. Heating and Confinement

The primary heating on MAST is provided by neutral beam injection which has been commissioned up to ~ 3MW, ~ 40keV operation in deuterium for typical pulse lengths of up to 300ms. Measurements with an E||B Neutral Particle Analyser (NPA), which can measure energies in the range 0.5 – 600keV/amu for both H and D, indicate that fast ion slowing down is classical [1]. Slowing down times are typically ~ 20 – 40ms but can be significantly longer at low density.

2.1. H-mode Access

H-mode access is routinely achieved in both Ohmic and neutral beam heated plasmas in MAST. The usual H-mode characteristics are observed [2], namely, a clear improvement in confinement, a steepening of the edge density gradient (leading to enhanced emission of mode

-converted electron Bernstein waves), a reduction in edge turbulence and an increase in edge poloidal rotation. Results confirm earlier observations in COMPASS-D [3] that inboard mid-plane gas puffing leads to improved H-mode access and quality. Stimulated by these observations, neo-classical theory has recently been extended to investigate the effect of a poloidal variation in the edge neutral density on the edge plasma flow [4]. It is found that, provided the neutral fraction n_0/n_i exceeds 10^{-4}, the radial transport of toroidal momentum due to charge exchange dominates neo-classical viscosity and can determine the toroidal plasma flow and radial electric field. Furthermore, the edge radial electric field and outboard toroidal flow velocity tend to be larger if the neutral atoms are concentrated at the inboard side. Such changes in the edge plasma flow could influence the formation of the edge transport barrier (ETB), this being favoured by an increase of edge flow shear which can stabilise plasma turbulence. Detailed edge profiles of the toroidal ion flow velocity $v_{\phi i}$ have been obtained in MAST from spectroscopic observations of helium ions, deposited in the plasma edge from a thermal helium jet at the outboard mid-plane, and show that compared with outboard puffing, inboard fuelling leads to increased flow velocities at the outboard mid-plane, in both L-mode and H-mode discharges, as predicted by the theory [5, 6]. These studies were carried out in Ohmic discharges to avoid complications due to the external toroidal momentum input associated with the neutral beams.

Studies of Ohmic H-mode plasmas (elongation $\kappa \sim 1.9$, triangularity $\delta \sim 0.37$) have also been used to explore the impact of the magnetic configuration on H-mode access [7]. MAST is usually operated in a double null divertor (DND) configuration with upper and lower X-points which do not necessarily lie on the same flux surface (Fig 1), giving rise to the distinction between lower DND (LDND), connected DND (CDND) and upper DND (UDND) configurations. Lower and upper here indicate the position of the active X-point. The departure from a CDND configuration may be characterised by the separatrix separation at the outboard mid-plane δ_{sep}. The configuration is regarded as connected if $|\delta_{sep}|$ is much less than the heat flux width in the scrape-off layer (SOL). Note that an exact CDND configuration does not correspond to a power balanced DND due to the influence of the ion ∇B drift, which in these experiments was directed downwards. The effect on H-mode properties of varying δ_{sep} has been investigated. Note that the position of the X-points relative to the nearest material surface changed by less than 2% as δ_{sep} was varied. Ohmic H-mode is only achieved when $|\delta_{sep}/\rho_i| \leq 0.5$, where ρ_i is the ion Larmor radius (typically $\rho_i \sim 6$mm), at the outboard mid-plane last-closed-flux-surface (LCFS), i.e. in a CDND configuration. In fact, similar conclusions also apply in neutral beam heated discharges. δ_{sep} is derived from EFIT reconstructions and validated by monitoring the power flow distribution to the divertor target plates (upper/lower, inner/outer). Although there

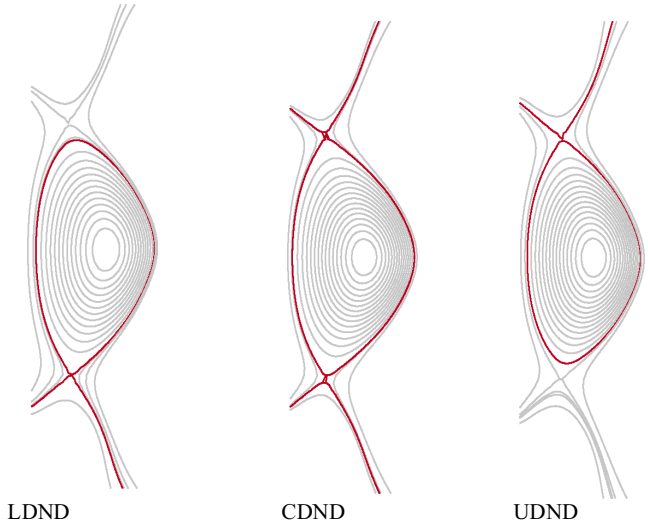

FIG. 1. DND configurations in MAST.

are substantial changes in the balance of power and particle fluxes between the various divertor targets as the magnetic configuration is varied from LDND to UDND, these changes are gradual. There is no evidence, for example, of significant changes in recycling or core impurity levels as $|\delta_{sep}/\rho_i|$ is varied in the region of 0.5 (except those resulting from the transition to or from H-mode) which could explain the higher L-H threshold for non-CDND configurations. Indeed, at present, there is no clear explanation of these observations, although it seems likely that they are linked to the large changes in parallel connection length in the scrape-off layer at the transition from CDND to UDND or LDND. It is interesting to note that in high triangularity ($\delta \sim 0.8$) DIII-D discharges, the L-H power threshold is also minimum for a DND configuration [8].

The low aspect ratio of MAST allows differentiation between different forms of the H-mode power threshold scaling. For example, results to date are clearly much better described by scaling laws of the form $P_{scal} \sim S$, where S is the plasma surface area, rather than $P_{scal} \sim R^2$. With optimised fuelling and magnetic configuration the power threshold data are on average a factor $P_{th,MAST}/P_{scal} \sim 1.7$ above the scaling law given by Ryter et al. [9], namely,

$$P_{scal} = 0.061 n_{20}^{0.53} B_T^{0.78} S^{0.84}$$

If we attribute this difference to an aspect ratio dependence (and not to other factors such as differences in divertor geometry), it would imply the need to introduce a dependence of the form $P_{scal} \propto \varepsilon^{0.5}$, where ε is the inverse aspect ratio. Detailed analysis requires a regression on the whole database.

2.2. H-mode Confinement

Energy confinement times in MAST generally lie in the range 20 – 80ms, although higher confinement times have been measured under more transient conditions. Kinetic (thermal plus fast ion energy) and magnetic (EFIT) evaluations of plasma stored energy agree within 10% over a wide range of discharge conditions [10]. The fast ion energy content is typically small, of order ~ 10%. To evaluate the fast ion stored energy including borderline adiabatic orbits, a newly developed, parallelised, version of the LOCUST Monte Carlo code [11] has been deployed, where electron drag, thermal ion scattering and energy diffusion are modelled.

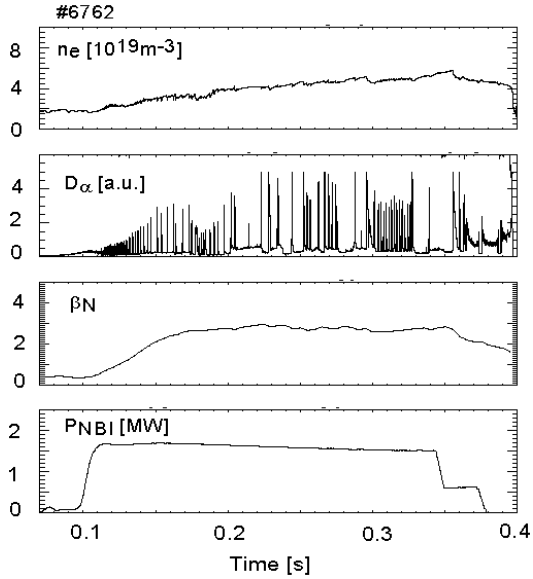

FIG. 2. Quasi-stationary ELMy H-mode: line-averaged density, D_α emission, normalised beta and neutral beam power. I_p = 0.73MA, B_T = 0.46T, deuterium plasma, deuterium NBI.

In order to compare MAST data with international scaling laws for ELMy H-mode confinement we have established a database of quasi-stationary discharges [12] in which the time-derivative of energy content dW/dt satisfies the condition,

$$-0.05 \leq (dW/dt)/P \leq 0.35$$

where P is the absorbed power, for a period $\geq 3\tau_E$. A typical example of a

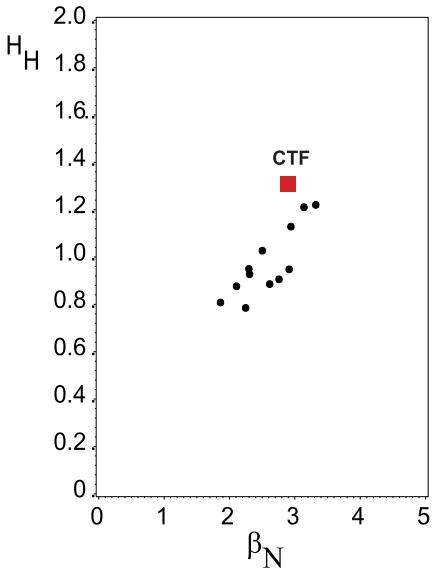

FIG. 3. Dataset of quasi-stationary ELMy H-mode discharges compared with the parameters of a CTF. The energy confinement time (normalised to IPB98(y,2)) is plotted against normalised beta.

quasi-stationary ELMy H-mode discharge is shown in Fig 2. The energy content is constant for about 200ms (~ $4\tau_E$), with β_N ~ 3 and $H_H^{IPB98(y,2)}$ ~ 1. The dataset of quasi-stationary ELMy H-mode discharges is illustrated in Fig 3 where it is seen that the values of the normalised parameters β_N and H_H simultaneously achieved are approaching those required for a Component Test Facility (CTF) based on an ST volume neutron source. The normalised density in these discharges ($\bar{n}_e/n_{Gr}$ ~ 0.5) significantly exceeds that required in the CTF. Density and temperature profiles typical of this dataset are shown in Fig 4, in this case for a discharge in which one of the two beam lines was operated in hydrogen, to increase charge exchange signals, in order to give a reliable ion temperature measurement over the whole profile.

It is noteworthy that confinement times broadly consistent with IPB98(y,2) scaling are obtained in MAST with ELMs that exhibit Type III characteristics, i.e. the ELM frequency f_{ELM} decreases with increasing power and decreasing density. Confinement does, however, degrade with increasing ELM frequency, as illustrated in Fig 5. At the lowest ELM frequencies confinement enhancement factors H_H can reach ~ 1.5. Stability analysis indicates that the pedestal parameters in some discharges are close to the high-n ballooning limit [13], where Type I behaviour might be expected, but the ELMs remain relatively benign (see section 4.1).

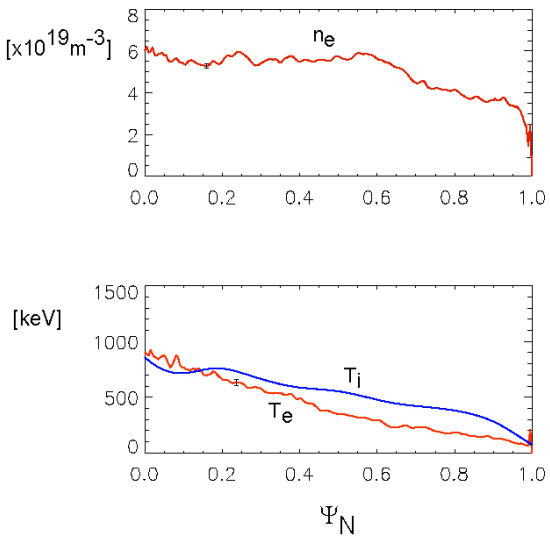

FIG. 4. Density and temperature profiles in a quasi-stationary ELMy H-mode discharge (#6953).

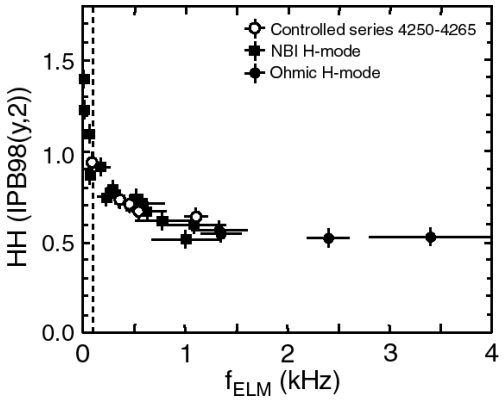

FIG. 5. Variation of energy confinement time (normalised to IPB98(y,2)) with ELM frequency f_{ELM}.

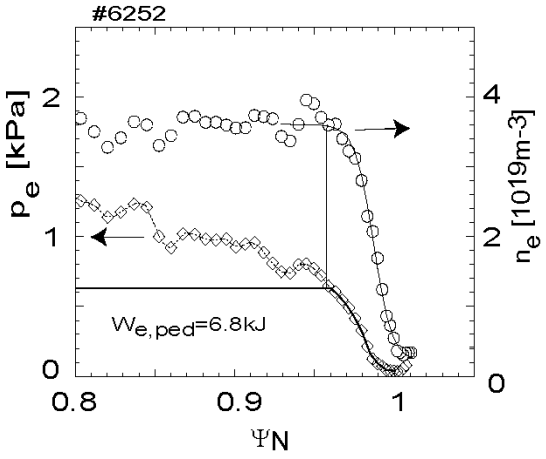

FIG. 6. Electron energy pedestal in a quasi-stationary ELMy H-mode discharge (#6252).

The MAST Thomson scattering system gives high spatial resolution measurements over the whole pedestal region allowing the electron pedestal energy to be accurately evaluated in a single discharge for comparison with pedestal scaling laws, such as that given by Thomsen et al. [14],

$$W_{ped,scal} = e^{-3.74} I_p^{1.71} R^{1.16} P^{0.31} M^{0.3} \left(\frac{q_{95}}{q_{cyl}} \right)^{1.2}$$

where the plasma current I_p is in MA, the loss power P is in MW and the effective mass M is in amu. This scaling is derived from a sub-set of 'medium aspect ratio' tokamaks with a small range of $\varepsilon = 0.24 - 0.37$. Pedestal measurements in a typical quasi-stationary MAST ELMy H-mode discharge are illustrated in Fig 6, [12]. The measured electron pedestal energy, $W_{e,ped} = 6.8$kJ is more than a factor x4 lower than predicted by the above scaling, $0.5W_{ped,scal} = 30$kJ. If we attribute this difference to an aspect ratio dependence it would imply a scaling approximately of the form $W_{ped,scal} \propto \varepsilon^{-2}$.

2.3. Internal Transport Barriers

There are strong indications that both particle and energy internal transport barriers (ITBs) have been observed in MAST [6]. NBI heating (~2MW) was applied throughout the plasma current ramp-up to limit current penetration, giving rise to weak central magnetic shear (EFIT). Operation at modest density ($\overline{n}_e \sim 1 - 3 \times 10^{19}$m^{-3}) ensured good beam penetration and high momentum input per particle in order to maximise flow shear. Example profiles of C^{6+} ion temperature and toroidal velocity from these discharges are shown in Fig 7. There is a marked increase in the ion temperature gradient in the region where the toroidal flow shear is greatest. The central ion temperature reaches a value in excess of 3keV and the toroidal flow velocity exceeds 200km/s in the core. A clear particle transport barrier is also observed and there is evidence of a steepening of the electron temperature gradient ($T_{e0} \sim$ 1.3keV) spatially coincident with the ion temperature gradient increase. Z_{eff} profile measurements indicate $Z_{eff} \sim 3$ over the core region of these discharges.

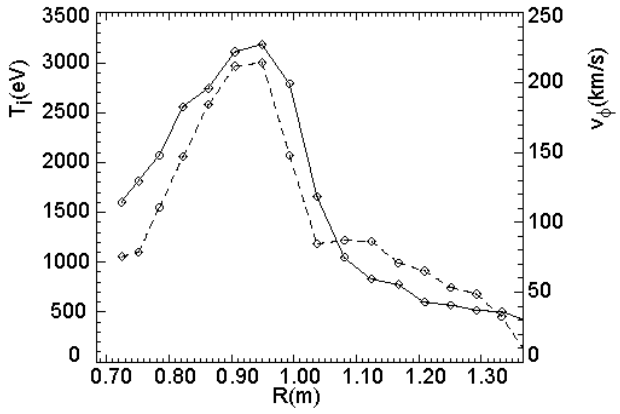

FIG. 7. Internal transport barrier formation in MAST: profiles of C^{6+} ion temperature (solid line) and toroidal velocity are shown (#7051).

3. High Beta and Plasma Stability

One of the key attributes of the ST is its capability of high beta operation, as confirmed in the START device [15], where values of toroidal beta up to $\beta_t \sim 40\%$ were obtained. Recent increases in beam power up to 3MW have allowed the first exploration of high beta discharges in MAST.

3.1. High Beta Performance

Toroidal beta values of up to $\beta_t \sim 16\%$ have so far been achieved with an injected beam power of 2.8MW at $I_p = 1.35$MA (Fig 8). The central electron temperature reached $T_{e0} = 1.7$keV in this discharge (#7107). The fast ion energy accounts for ~ 20% of the total stored energy. At reduced plasma current, values of normalised beta and poloidal beta up to $\beta_N \sim 5.3$, $\beta_p \sim 1.7$

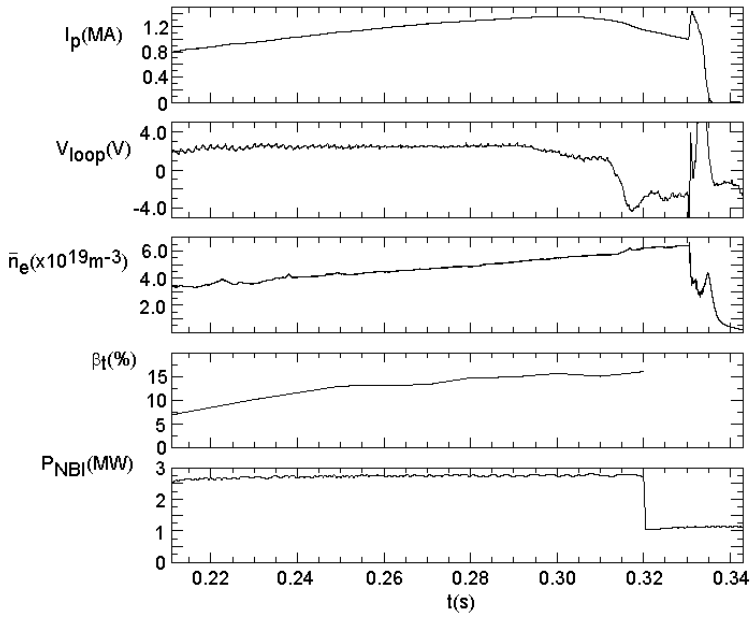

FIG. 8. High beta discharge in MAST (#7107).

have been simultaneously achieved ($\beta_N > 5l_i$) and $\beta_N > 4$ has been sustained for > 100ms. Stability analysis suggests that these discharges are approaching the ideal n=1 no wall external kink stability limit [16]. However, there is no obvious MHD limit to performance. Typical parameters are $T_{e0} \sim 1$keV, $T_i/T_e \sim 1.5$, $n_{e0} \sim 5 \times 10^{19}$m^{-3} with $P_{NBI} \sim 2.8$MW. The fast ion energy accounts for ~ 15 - 20% of the total stored energy in these discharges and the bootstrap fraction is estimated to be ~ 40 - 50%.

3.2. Neo-classical Tearing Modes

In the discharges with highest β_t and highest β_N sawteeth were absent or small and neo-classical tearing modes (NTMs) were avoided. However, by operating in regimes with large sawteeth and high β_p, low order (m/n = 3/2, m/n = 2/1) NTMs have been observed [16, 17]. So far, no higher order modes (e.g. m/n = 4/3) have been seen. A typical discharge is illustrated in Fig 9. Here successive sawteeth excite small decaying n = 2 modes which briefly reduce β_p. However, when a high enough β_p is reached, a sawtooth excites a longer lived 3/2

mode which produces a greater and more sustained β_p decrease. Eventually β_p recovers when the island size has decreased after an L-H transition. As β_p increases further, however, a 2/1 NTM is eventually excited. Typical island widths in MAST are ~ 4cm for the 3/2 mode and ~ 10cm (15 - 20% of the minor radius) for the 2/1 mode. These values are calculated from magnetic measurements and confirmed by the high spatial resolution Thomson scattering system, the results from which clearly exhibit profile flattening. The 3/2 mode typically results in a decrease in confinement of ~ 10%, in approximate agreement with the Chang and Callen belt model [18]. The 2/1 mode can trigger a transition to L-mode, sometimes followed by mode locking and disruption.

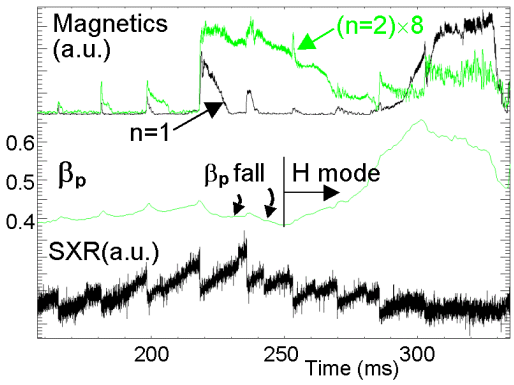

FIG. 9. Sawtooth triggered neo-classical tearing modes (m/n = 3/2, m/n = 2/1) in MAST (#2941): centre column magnetics signals, poloidal beta, soft x-ray emission.

Generally the 3/2 NTM is excited on MAST close to its saturated size and at β_p values close to the critical β_p for mode growth ($\beta_p \sim 0.4$). This indicates a strong seeding process in the ST, due to the large sawtooth inversion radius and the strong toroidal coupling between modes. Detailed numerical modelling of the 3/2 island evolution reproduces mode behaviour well [16, 17], confirming the significance of stabilising field curvature effects which cancel out about 60% of the bootstrap drive in these discharges. This highlights a potential route for optimising stability to the NTM in the spherical tokamak by exploiting its strong shaping capabilities. It is also necessary to include small island stabilisation effects (ion polarisation effects and/or finite island transport) to explain the strong decay in amplitude as β_p falls.

3.3. Fast Particle MHD

Discrete Alfvénic activity up to 450kHz has been observed in neutral beam heated discharges ($E_{beam} > 35$keV) for both H ($v_{||}/v_A \sim 1.7$) and D ($v_{||}/v_A \sim 1$) injection, where $v_{||}$ is the beam velocity and v_A is the Alfvén velocity at the magnetic axis [19]. High frequency activity is observed in both the TAE ($f_{TAE} = v_A/(4\pi Rq)$) and EAE ($f_{EAE} = v_A/(2\pi Rq)$) frequency ranges. Both steady-state and, more commonly, chirping activity has been observed and simultaneous up/down chirping has been seen. Fishbone activity, as observed in START [20], has also been observed in MAST. In Ohmic plasmas, high frequency Alfvénic activity at low amplitude has been measured with n = 0, consistent with excitation of GAE modes [21]. Under present MAST conditions, fast particle driven MHD activity is relatively benign.

4. Plasma Exhaust

Plasma exhaust is a critical issue for the ST due to the small wetted area of the inboard divertor targets. As in conventional tokamaks, the impact of ELMs is of particular concern. MAST is well equipped with edge plasma diagnostics [22, 23]. Of particular note are the extensive arrays of high spatial and temporal resolution Langmuir probes covering all four targets in DND operation. The fast sweep (65μs) on each individual probe allows data to be

resolved in periods much shorter than an ELM duration. In evaluating the power to the probes, $T_i = T_e$ is assumed. For L-mode and ELMy H-mode regimes the total power to all four targets typically accounts for > 80% of the power estimated to be flowing from the plasma core, allowing for radiation and changes in stored energy. This fraction does appear to fall somewhat during long inter-ELM periods, possibly as a result of an increase in SOL ion temperature and a corresponding rise in power flowing in the ion channel, to which the target probes are insensitive.

4.1. Divertor Power Loading and ELMs

Fortunately, detailed divertor power loading studies have shown a strong bias of power efflux towards the outboard targets where the wetted area is greatly increased (x50 in MAST) over that on the inboard side [22, 23, 24]. This is illustrated in Fig 10. For discharges with high frequency ELMs, the outboard – inboard target power ratio P_{out}/P_{in} exceeds 30 during ELM events (implying that > 96% of the power flowing to the targets flows to the outboard side), falling to ~ 10 between ELMs (>90% to outboard side). P_{out}/P_{in} decreases as the ELM frequency decreases but still remains above 15 (>93% to outboard side) during ELM events. For long inter-ELM periods however, the ratio decreases to ~ 4, comparable with the ratio of surface areas of the outboard and inboard separatrices (indicated by the dashed line in Fig 10). For L-mode discharges in a connected DND configuration, P_{out}/P_{in} reaches values comparable with those during ELM events. These data are consistent with losses from the core being driven by poloidally symmetric processes during inter-ELM periods, and thus distributed according to the separatrix area ratio, whereas during L-mode and at ELM peaks, the transport is presumably enhanced by poloidally asymmetric processes more prominent on the low field, bad curvature outboard side.

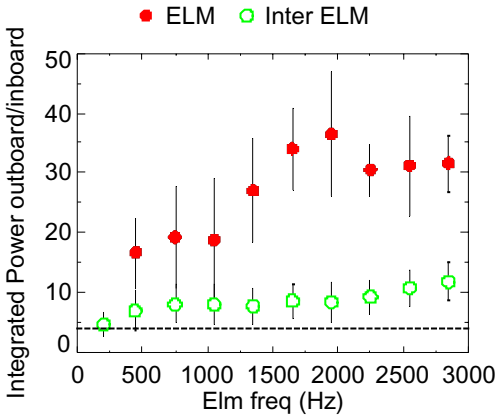

FIG. 10. Ratio of spatially integrated power to the outboard and inboard divertor targets versus ELM frequency.

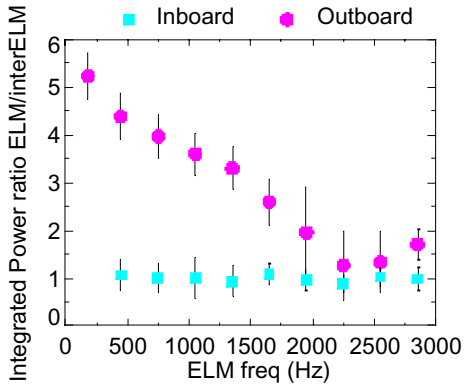

FIG. 11. Ratio of the spatially integrated power at an ELM to that between ELMs for the inboard and outboard strike points as a function of ELM frequency.

Fig 11 shows a plot of the ratio of the spatially integrated (over the target area) power arriving at the ELM to that arriving between ELMs as a function of ELM frequency for the outboard and inboard strike-points. Firstly, independent of frequency the ratio is ~ 1 for the inboard strike-points consistent with very little of the power released by the ELMs reaching the inboard targets. For the outboard targets the ratio increases with decreasing ELM frequency

reaching an average ratio of greater than 5 for ELMs below 250 Hz. The maximum peak power densities observed to date during an ELM, for powers flowing to the SOL of up to 2MW, are $2MWm^{-2}$ at the inboard strike-points and $4MWm^{-2}$ at the outboard strike-points. The outboard strike points shift radially outwards by 2 - 3 cm during low frequency ELMs, but there is no significant broadening of the target power deposition.

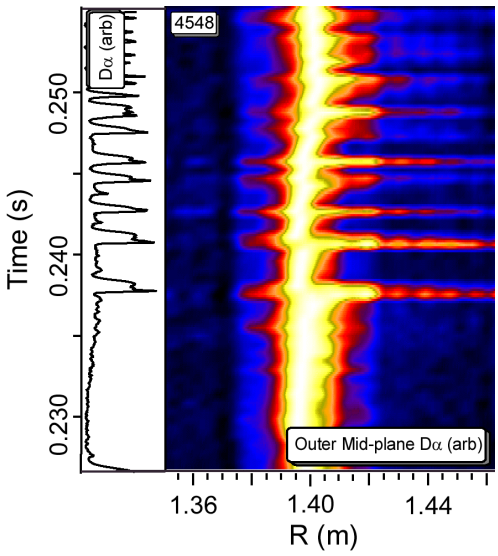

FIG. 12. A tomographically inverted false colour image of D_α emission from the outboard midplane during an ELMy H-mode discharge together with the corresponding divertor D_α signal.

ELM energy losses ΔW_{ELM} are less than 4% of the stored energy in all regimes explored so far. ΔW_{ELM} is strongly correlated with the pedestal density [22] and the effect on pedestal profiles is consistent with ΔW_{ELM} being dominated by convective losses from the pedestal region. During an ELM, the pedestal density profile exhibits a broad tail on the outboard side extending well beyond the inter-ELM separatrix. Measurements with a reciprocating probe and a linear D_α camera (Fig 12) routinely indicate ELM power effluxes extending 30cm beyond the separatrix. This phenomenon appears to be consistent with the radial expansion of a poloidally localised structure at > 1km/s [22, 23].

4.2 Studies of Divertor Power Reduction

Reduction of target power loads by radiative detachment is being explored in MAST. The roll-over and then decrease of the divertor ion flux and temperature for $\bar{n}_e > 3.5\times10^{19}\ m^{-3}$ has been observed for both Ohmic and L-mode plasmas [25]. Detachment was achieved at all four targets, despite the fully open nature of the MAST divertor and horizontal outboard targets. Target plasma densities at roll-over are substantially lower than has been reported in other tokamaks but the existence of detachment is supported by a strong increase in the D_γ/D_α ratio.

Toroidally asymmetric biasing of divertor components in a tokamak has been proposed [26, 27] as a means of broadening the target heat flux width by the generation of convective cells. Initial experiments have been carried out in MAST to test this concept [22]. The biasing has a strong effect on target D_α and ion saturation current profiles. Initial analysis shows a significant broadening of the D_α profile on the biased components and a reduction in the total power to the un-biased components.

4.3. Plasma Terminations and Halo Current Measurements

It is well-known that STs exhibit a certain resilience to major disruptions. Under circumstances in which the plasma in a conventional tokamak would disrupt, the ST plasma often undergoes an internal reconnection event (IRE) instead, from which it is able to recover.

Nevertheless, IREs can sometimes lead to a vertical displacement event (VDE) and a rapid plasma termination. After an IRE, the ion distribution is observed to have a pronounced high energy tail extending to a few keV. This has been attributed to the large toroidal electric field which develops as the plasma lowers its magnetic energy while conserving its helicity [28].

MAST is equipped with extensive halo current diagnostics; comparison of sinks and sources indicates that all halo currents are measured. Under normal ST operation with $I_p > 350$kA, halo current fractions I_h/I_p are ≤ 25%. Halo current asymmetries are also small with I_h/I_pxTPF < 0.3 (TPF = toroidal peaking factor), well below the ITER design limit. There is a tendency for the measured TPF to increase with major radius, implying that toppling/bending forces may be less severe in the high field region than might have been anticipated; this might also explain the lower average TPF seen in STs compared to conventional devices. Furthermore, recent studies [23, 29] have demonstrated that during a VDE the plasma behaves more as a voltage source than a current source, indicating that it may be possible to determine the preferred halo current path and limit the halo current in sensitive components by adjusting the resistance in a particular path.

5. Plasma Current Generation

5.1. Non-solenoid Operation

Plasma current ramp-up and sustainment, without using a central solenoid, is a key issue for the ST since it is not possible to accommodate such a component in an ST power plant. The design of MAST, in which the poloidal field coils are mounted inside the vacuum vessel, allows exploitation of innovative start-up techniques such as the plasma 'merging-compression' scheme. This approach has been used to establish plasmas with currents approaching 0.5MA, without use of flux from the central solenoid. The low inductance and high poloidal beta of an ST plasma mean that the increase in vertical field required to maintain plasma equilibrium, during neutral beam heating, provides an effective contribution to plasma current induction. For example, a plasma current of > 0.6MA has been sustained for 0.2s with constant solenoid current, during high power NBI, due to a combination of vertical field ramp-up, neutral beam current drive and a significant bootstrap fraction (~ 40%) [30].

5.2. Non-inductive Current drive

Preliminary neutral beam current drive experiments, using both co - and counter – injection, have been carried out at $I_p \sim 350$kA, $n_{e0} < 1.5 \times 10^{19}$m^{-3} with $P_{NBI} \leq 2$MW. Under these conditions, calculations using LOCUST predict a central beam driven current $I_{beam} \sim 90$kA. Compared with co-injection, counter-injection results in higher q(0), lower l_i and substantially higher loop voltage for similar plasma temperature, as expected. Preliminary analysis suggests a beam driven current comparable with code predictions.

6. Summary and Conclusions

MAST data are making important contributions to key physics R & D issues for ITER, as well as helping to establish the viability of the ST concept as a future fusion materials test facility and/or power plant. Key results include: the establishment of good confinement with relatively benign ELMs; indications of both particle and energy internal transport barriers; a strong bias of power efflux to the outboard divertor targets where it is more easily handled;

sustainment of discharges at high normalised beta ($\beta_N > 5$) close to the ideal no wall stability limit; confirmation of the stabilising role of field curvature effects in the evolution of neo-classical islands; low halo current magnitudes and asymmetries; the beneficial effects of toroidally asymmetric divertor biasing and promising indications of neutral beam current drive. Together with the extensive array of high quality diagnostics on MAST, these results provide an excellent platform for further input to key ITER physics studies and issues of specific relevance to the viability of the ST concept.

Acknowledgements
This work was jointly funded by the UK Dept. of Trade and Industry and Euratom. The NBI equipment is on loan from ORNL, the NPA from PPPL, pellet diagnostics from ENEA and the pellet injector, built at Risø, was supplied by FOM.

References
[1] BYROM, C., et al., Proc. 28th Conf. Contr. Fus. & Plas. Phys., ECA **25A** (2001) 585
[2] AKERS, R.J., et al., Phys. Rev. Lett. **88** (2002) 035002
[3] VALOVIC, M., et al., Plasma Phys. Contr. Fusion, **44** (2002) A175
[4] FÜLÖP, T.M., et al., these proceedings (Paper TH/P3-03)
[5] FIELD, A., et al., Proc. 29th Conf. Contr. Fus. & Plas. Phys., ECA **26B** (2002) P-1.114
[6] CAROLAN, P.G., et al., these proceedings (Paper EX/C2-6)
[7] MEYER, H., et al., Proc. 29th Conf. Contr. Fus. & Plas. Phys., ECA **26B** (2002) P-1.056
[8] CARLSTROM, T.N., et al., Bull. Am. Phys. Soc. **46** (2001) 220
[9] RYTER, F., et al., Plasma Phys. Contr. Fusion **44** (2002) A415
[10] AKERS, R.J., et al., Proc. 28th Conf. Contr. Fus. & Plas. Phys., ECA **25A** (2001) 581
[11] AKERS, R.J., et al., Nuc. Fus. **42** (2002) 122
[12] VALOVIC, M., et al., Proc. 29th Conf. Contr. Fus. & Plas. Phys., ECA **26B** (2002) P-1.054
[13] COUNSELL, G.F., et al., Proc. 29th Conf. Contr. Fus. & Plas. Phys., (2002) I-1.04, to be published in Plasma Phys. Contr. Fusion
[14] THOMSEN, K., et al., Plasma Phys. Contr. Fusion **44** (2002) A429
[15] GRYAZNEVICH, M.G., et al., Phys. Rev. Lett. **80** (1998) 3972
[16] BUTTERY, R.J., et al., these proceedings (Paper EX/S1-6)
[17] BUTTERY, R.J., et al., Phys. Rev. Lett. **88** (2002) 125005
[18] CHANG, Z. & CALLEN, J.D., Nuc. Fus. **34** (1994) 1309
[19] HOLE, M., et al., Proc. 29th Conf. Contr. Fus. & Plas. Phys., ECA **26B** (2002) O-2.02
[20] McCLEMENTS, K.G., et al., Plasma Phys. Contr. Fusion **41** (1999) 661
[21] McCLEMENTS, K.G., et al., these proceedings (Paper TH/P3-17)
[22] COUNSELL, G.F., et al., Proc. 15th Conf. on Plasma Surface Interactions (2002) I-15
[23] COUNSELL, G.F., et al., these proceedings (Paper EX/D1-2)
[24] KIRK, A., et al., Proc. 15th Conf. on Plasma Surface Interactions (2002) P3-74
[25] TABASSO, A., et al., Proc. 15th Conf. on Plasma Surface Interactions (2002) P1-61
[26] COHEN, R.H., et al., Nucl. Fusion **37** (1997) 621
[27] RYUTOV, D.D., et al., Plasma Phys. Contr. Fusion **43** (2001) 1399
[28] HELANDER, P., et al., these proceedings (Paper TH/8-1)
[29] MARTIN, R., et al., Proc. 29th Conf. Contr. Fus. & Plas. Phys., ECA **26B** (2002) P-1.053
[30] SYKES, A., et al., Proc. 19th Symposium. on Fusion Engineering (2002) p454,